

Responses of the Martian magnetosphere to an interplanetary coronal mass ejection: MAVEN observations and LatHyS results

N. Romanelli¹, R. Modolo¹, F. Leblanc², J-Y. Chaufray¹, A. Martinez¹, Y. Ma³, C. O. Lee⁴, J. G. Luhmann⁴, J. Halekas⁵, D. Brain⁶, G. DiBraccio⁷, J. Espley⁷, J. McFadden⁴, B. Jakosky⁶, Mats Holmström⁸.

Corresponding author: N. Romanelli, Laboratoire Atmosphere, Milieux et Observations Spatiales (LATMOS), IPSL, CNRS, UVSQ, UPMC, Tour 45-46, 4 place jussieu, 75252 Paris cedex 05, Paris, France. (Norberto.Romanelli@latmos.ipsl.fr) orcid.org/0000-0001-9210-0284

¹Laboratoire Atmosphere, Milieux et Observations Spatiales (LATMOS), IPSL, CNRS, UVSQ, UPMC, Paris, France.

²LATMOS/IPSL, UPMC, Univ Paris06 Sorbonne Universités, UVSQ, CNRS, Paris, France.

This article has been accepted for publication and undergone full peer review but has not been through the copyediting, typesetting, pagination and proofreading process, which may lead to differences between this version and the Version of Record. Please cite this article as doi: 10.1029/2018GL077714

The Mars Atmosphere and Volatile Evolution (MAVEN) spacecraft observed a strong interplanetary coronal mass ejection (ICME) reaching Mars on 13 September 2017. In this work we analyze the interaction between such an extreme event and the Martian induced magnetosphere by means of LAT-MOS Hybrid Simulation (LatHyS) stationary runs and magnetic field and plasma observations obtained by MAVEN in a time interval from ~ 5 h before the ICME shock arrival to about 5.5 h after the impact. Detailed comparisons between simulation results and such MAVEN measurements are per-

³Department of Earth Planetary and
Space Sciences, UCLA, Los Angeles,
California, USA.

⁴Space Sciences Laboratory, University of
California, Berkeley, California, USA.

⁵Department of Physics and Astronomy,
University of Iowa, Iowa City, Iowa, USA.

⁶Laboratory for Atmospheric and Space
Physics, University of Colorado, Boulder,
Colorado, USA.

⁷NASA Goddard Space Flight Center,
Greenbelt, Maryland, USA.

⁸IRF, Kiruna, Sweden.

formed and show that several stages during this interaction can be described through a combination of steady states. LatHyS results show the simulated bow shock is closer to the planet for higher magnetosonic Mach number and solar wind dynamic pressure conditions, in agreement with previous observational studies. MAVEN observations and LatHyS results also suggest a compression on the flanks of the magnetic pile-up boundary. Finally, simulated H^+ and O^+ planetary escape rates increase by a factor ~ 10 and ~ 2.4 , respectively, due to the ICME passage through the Martian magnetosphere.

Keypoints:

- The interaction between an ICME and Mars is studied by means of MAVEN observations and LatHyS stationary runs.
- A characterization of the bow shock compression during this event is performed, based on LatHyS results.
- During the analyzed event, simulated H^+ and O^+ planetary loss rates increase by a factor ~ 10 and ~ 2.4 , respectively.

1. Introduction

Interplanetary coronal mass ejections (ICMEs) are large-scale magnetic field and plasma structures with enhanced field magnitude with respect to magnetized background solar wind (SW), and with plasma properties distinct from the solar wind in which they are embedded [e.g., Gopalswamy, 2006; Jian et al., 2008]. Given their known capability to generate major geomagnetic storms at Earth [e.g., Gosling et al., 1991; Tsurutani and Gonzalez, 1997], and the more direct interaction that takes place between the SW and planets lacking an intrinsic global magnetic field (such as Venus and Mars) [Russell et al., 1980; Acuña et al., 1998], ICMEs are expected to play an important role modifying the plasma environment surrounding these atmospheric obstacles.

Studying the Martian response to variable external conditions is of great importance, particularly to identify and characterize time-dependent physical processes occurring inside and around its induced planetary magnetosphere. These studies allow, for instance, to quantify different magnetospheric recovery timescales, to determine related temporal variabilities in each atmospheric escape channel and to estimate the role that planetary neutral and ion escape to space might have played throughout the history of this planet. However, despite the progress in the understanding of this planetary plasma environment, studies on the responses of the induced magnetosphere of Mars to variability in the external conditions are still required. This is due to the proper limitations of localized spacecraft observations and instrumental design, the computationally expensive time-dependent numerical simulation calculations, and the large amount of non-linear time-dependent physical processes taking place in such interaction.

The interaction between large ICMEs and the Martian magnetosphere has been studied based on observations provided by Mars Global Surveyor, Mars Express and Mars Atmosphere and Volatile Evolution (MAVEN) [Jakosky et al., 2015a] missions. Results from such investigation can be found in Crider et al. [2005]; Edberg et al. [2010]; Futaana et al. [2008]; Morgan et al. [2014]; Jakosky et al. [2015b]; Curry et al. [2015]; Dong et al. [2015]; Sánchez-Cano et al. [2017]; Ma et al. [2017]. Among these studies, Jakosky et al. [2015b] have shown that ICMEs are capable of increasing the atmospheric planetary escape rate by approximately a factor 10, compared to nominal solar wind conditions. Consistently with this work, Ma et al. [2017] performed time-dependent MHD numerical simulations to analyze the rapid changes that took place in the plasma environment around Mars due to these disturbances in the solar wind and showed that ion escape rates increase by more than one order of magnitude during such event.

In the present work we study the interaction between an ICME that impacted the Martian magnetosphere around 13 September 2017, by means of MAVEN magnetic field and plasma observations. In addition, we also make use of the LATMOS Hybrid Simulation (LatHyS), the Laboratoire de Météorologie Dynamique Global Climate Model (LMD-GCM) and the Exospheric Global Model (EGM) codes to describe the Martian atmosphere, ionosphere and magnetosphere during this time interval and to study the response of this induced magnetosphere to such extreme event. To do this, we perform three stationary hybrid simulations under estimated external conditions (MAVEN was inside the magnetosphere during this time interval) characterizing different stages of this interacting system. Analysis of Mars Express plasma data during this event is beyond

the scope of the present study and will be considered in a future study. After providing a brief description of MAVEN Magnetometer (MAG), Solar Wind Ion Analyzer (SWIA) and Supra-Thermal and Thermal Ion Composition (STATIC) capabilities and the LatHyS code (Section 2), we perform a comparison between MAVEN observations and LatHyS results along the spacecraft trajectory in Section 3. We also study the response of the Martian bow shock (BS) and the Magnetic Pile-up Boundary (MPB) to the changes in the external conditions due to the passage of the ICME around the induced magnetosphere of Mars. In addition, we estimate the planetary H^+ and O^+ loss rates during this event. In Section 4 we provide our conclusions.

2. MAVEN instruments and LatHyS code

The MAG instrument provides vector magnetic field measurements with two independent fluxgate magnetometers placed on the end of the solar array panels. They possess a broad range (up to 65,536 nT per axis), a maximum sampling frequency of 32 Hz and accuracy of ~ 0.25 nT [Connerney et al., 2015a, b]. In this work we have used full time resolution MAG data.

SWIA is an energy and angular ion spectrometer covering an energy range between 25 eV/q to 25 keV/q (with 48 logarithmically spaced energy steps) with a field of view (FOV) of $360^\circ \times 90^\circ$ [Halekas et al., 2015]. In this work we used derived mean plasma density and bulk velocity with 8 s resolution.

STATIC is an energy, mass, and angular ion spectrometer, covering an energy range between 0.1 eV/q to 30 keV/q with a FOV of $360^\circ \times 90^\circ$ and a mass range from 1 to 70

amu [McFadden et al., 2015]. In this study we have used derived densities for H^+ , O^+ , O_2^+ and CO_2^+ (from the c6 data product) with 4 s resolution.

LatHyS is a global three-dimensional multispecies parallelized hybrid model that allows to describe plasma processes taking place in several space plasma environments [Modolo et al., 2005, 2012; Richer et al., 2012; Modolo et al., 2016; Leclercq et al., 2016]. Applied to the Martian environment, it treats six ion species kinetically: solar wind H_{sw}^+ and He_{sw}^{++} , and planetary H^+ , O^+ , O_2^+ , and CO_2^+ . The electrons are described by means of two massless fluids with different temperatures (solar wind and ionospheric) that ensure the quasi-neutrality condition. The planetary ions are the result of three ionization processes acting on the Martian atmosphere/exosphere (photoionization, charge exchange, and electron impact), several chemical reactions taking place at low altitudes and the self-consistent dynamics (of the ions) by considering model cross sections and ionization frequencies. The description of the crustal magnetic fields at Mars [Acuña et al., 1999] is based on the model derived in Cain et al. [2003]. A detailed description of the LatHyS model can be found in Modolo et al. [2016] and references therein. The description of the neutral and ionospheric Martian environment that affect, among other things, the mass-loading conditions of the solar wind is derived making use of the 3D LMD-GCM [González-Galindo et al., 2009; Chaufray et al., 2014, 2015] and the 3D EGM [Leblanc et al., 2017a, b].

In this work we perform three stationary numerical simulation runs with 80 km spatial resolution and a time step equal to $0.0333 \Omega_{ci}^{-1}$ where Ω_{ci} is the proton gyrofrequency of the undisturbed SW. The simulation domain extends from -2.4 to $2.4 R_M$ in X_{MSO} axis and

from -4.5 to $4.5 R_M$ in Y_{MSO} and Z_{MSO} axes (R_M stands for Martian radii, $1 R_M = 3393$ km). The Mars Solar Orbital (MSO) coordinate system is centered at Mars and is defined as follows: the X axis points toward the Sun, the Z axis is perpendicular to Mars's orbital plane and is positive toward the ecliptic north. The Y axis completes the right-handed system. Given that MAVEN is inside the Martian bow shock during the analyzed time interval, external conditions for the simulation runs are estimated based on MAVEN magnetosheath (MSH) measurements. Considered values for solar wind density (n_{SW}), mean velocity (U_{SW}), the Interplanetary Magnetic Field (IMF) and the magnetosonic Mach number for each simulation are shown in Table 1 [Ma et al., 2018]. These values, also considered for the three steady-state cases analyzed by Ma et al. [2018], are estimated mainly based on penetrating proton measurements [Halekas et al., 2015, 2017]. For a more detailed description on this aspect the reader is refer to Sections 3 and 4 of Ma et al. [2018]. When it comes to the crustal magnetic fields it is also worth pointing out that, for each of the three stationary simulations, we have fixed the subsolar GEO latitude and longitude at the values taken at MAVEN's closest approach (CA) during the corresponding time interval. The time interval described by each of these simulations is also reported in this Table. The 3-D description of the density, velocity, and temperature of the main neutral and ion species in Mars' thermosphere/ionosphere are determined for solar longitude $L_s = 90^\circ$ and mean solar activity, using the LMD-GCM. Moreover, these outputs are also used to define the background atmosphere and ionosphere of EGM, and to define Mars' atmosphere in LatHyS model. The reconstructed exospheric composition and density by EGM is used to describe Mars' exosphere in LatHyS model. Although a

peak in the Lyman-alpha and in the 0-7 nm MAVEN EUV channels are detected on 10 September 2017 between 16:02 and 16:12:45 UT [Thiemann et al., 2018], previous works making use of the LMD-GCM code [Chaufray et al., 2014, 2015] suggest effects associated with such local maximums do not significantly affect the outcome of LatHyS simulations for the time interval of the present study.

3. MAVEN observations and LatHyS results

3.1. Comparison along MAVEN's trajectory

Figure 1 displays magnetic field and plasma data obtained by MAVEN MAG, SWIA and STATIC instruments as a function of time, between 12 September 2017 22:00 UT and 13 September 2017 08:20 UT. From top to bottom, this Figure displays the magnetic field vectors in MSO coordinates, total field magnitude, mean plasma velocity components (from SWIA) in MSO coordinates, total plasma velocity, and ion densities derived from STATIC and SWIA. Each panel also shows the corresponding LatHyS results (from the three stationary simulations) along MAVEN's trajectory. As shown in Table 1, the mean IMF considered for the time interval associated with Simulation 1 is $\mathbf{B} = [0, -3, 0]$ nT, that is, a background magnetic field with nominal magnitude upstream from Mars. Moreover, the SW bulk velocity and density corresponding to this time interval are assumed to be $\mathbf{U}_{SW} = [-426, 0, 0]$ km/s and $n_{SW} = 1.9 \text{ cm}^{-3}$, respectively. Initially, MAVEN is located close to the terminator plane and inside the Martian magnetosheath. It measures strong wave activity, relatively high magnetic field magnitude (~ 6 nT) and plasma density ($\sim 4 \text{ cm}^{-3}$) and smaller plasma bulk velocity (~ 240 km/s). As MAVEN moves towards CA at around 12 Sept 22:54:29 UT, it measures an increase in the magnetic field intensity

due to the IMF pile-up and the presence of crustal magnetic fields. In addition, a strong decrease in the local plasma velocity and an increase in the total ion density with the major contributions coming from O_2^+ and CO_2^+ are observed. After reaching CA (altitude ~ 150 km), MAVEN is located downstream and crosses the MPB at the dawn flank at around 23:27 UT, time after which large fluctuations in both magnetic field and mean plasma velocity and density are, once again, detected. Consistent with this transition, STATIC mass spectrogram shows the presence of heavy ions approximately up to this time (not shown in this paper). Even though LatHyS does not capture the fluctuations in \mathbf{B} , \mathbf{U} and n observed in the Martian magnetosheath, the predicted profiles along the spacecraft trajectory are in good agreement with the observed mean values of each of them. Moreover, the IMF draping and pile-up, the crustal magnetic fields and correlated changes in the mean plasma velocity field and total plasma density are also well reproduced by LatHyS. These results therefore suggest that MAVEN observations between 12 Sept 22:00 UT and 13 Sept 02:52 UT can be understood in terms of nominal draping of magnetic field lines [see, e.g., Chacko and Hassam, 1997; Ma et al., 2004; Modolo et al., 2012; Romanelli et al., 2014, 2015; Naor and Keshet, 2015] and acceleration plasma processes [see, e.g., Dubinin et al., 2011; Halekas et al., 2017], assuming the external conditions reported in Table 1 (Simulation 1).

As can be seen in MAVEN Solar Energetic Particle data, the ICME shock reached the Martian environment at 13 Sept 02:52 UT [Lee et al., 2018]. As a result of subsequent changes in the external conditions associated with such extreme event (e.g., increase in the solar wind dynamic pressure and IMF magnitude), MAVEN observed magnetic field

magnitudes significantly larger (maximum being 112.8 nT) around CA (at 13 Sept 03:20:36 UT), compared with the previous orbit. This increment is not associated with crustal magnetic fields (according to Cain's model [Cain et al., 2003], they are not expected to exceed 15 nT magnitude in this case), but rather associated with a more intense magnetic pile-up and draping. As shown in Table 1, we model the 13 Sept 02:52 - 05:10 UT time interval by means of a stationary LatHyS run with $\mathbf{B} = [0, -10, 0]$ nT, $\mathbf{U}_{SW} = [-824, 0, 0]$ km/s and $n_{SW} = 4 \text{ cm}^{-3}$. Under these external conditions, LatHyS reproduces very well these signatures as well as the deceleration of the plasma and the increase in the total plasma density when MAVEN approaches the ionosphere. After CA, MAVEN observations suggest the spacecraft is inside the MPB until $\sim 03:36$ UT. Indeed, although fluctuations in the magnetic field are important even close to CA, heavy ions are not detected after this time (STATIC mass spectrogram). The observed values of the magnetic field components inside the MPB and the MSH (up to 05:10 UT) are well described under a nominal and stationary IMF draping picture (with the major component along the $-\mathbf{Y}_{MSO}$ axis). Moreover, predicted mean plasma velocities and total densities are also in good agreement with MAVEN SWIA and STATIC measurements during the time interval related to Simulation 2 (see Table 1). However, it is important to notice that physical processes taking place on different timescales are likely present and modify the Martian magnetosphere response to the ICME, when compared to that of under steady-state conditions. In particular, the main differences between observations and simulations (between 02:57 - 03:08 UT and 03:35-04:00 UT) are examples of such modifications, likely associated with a transient state of the plasma that can only be properly reproduced

through time-dependent numerical simulations. In agreement with this idea, simulation results by Ma et al. [2018] suggest MAVEN plasma field velocity during such time intervals can be related to variability in the SW velocity.

At Sept 13 05:10 UT a sharp change in the local magnetic field B_y polarity and an increase in the H^+ density are measured by MAVEN. Consistent with these observations, we perform a third stationary numerical simulation with the external conditions presented in Table 1 ($\mathbf{B} = [0, 10, 5]$ nT, $\mathbf{U}_{SW} = [-824, 0, 0]$ km/s and $n_{SW} = 12 \text{ cm}^{-3}$). MAVEN observes again a magnetic field configuration consistent with magnetic field draping and pile-up under the latter considered IMF orientation and increased solar wind density. For instance, it is worth noticing the opposite polarity of the B_x and B_y magnetic field components surrounding the Martian's ionosphere, compared to that of observed during the previous orbit. This is clearly consistent with the considered change in the IMF direction. Also, the higher magnetic pile-up (compared with the previous orbit) can be related to the expected increase in n_{SW} . As in the case of the two previous simulations, the total density predicted by LatHyS along MAVEN's trajectory is very close to that of the dominant species at different times. Indeed, total densities predicted by LatHyS in the Martian ionosphere are in very good agreement with the observed heavy ion densities (for example, for the maximum in the O_2^+ and/or CO_2^+ densities). Analogously, total density values predicted by LatHyS are in good agreement with protons densities measured by MAVEN when outside of the ionosphere. It is also interesting to notice that LatHyS is capable of reproducing very well the observed changes in the U_y and U_z components, resulting from accelerating processes taking place mainly in the flanks of the Martian

magnetosheath. In addition, it is worth pointing out that the presence of high energetic particle fluxes during part of the analyzed event generate an appreciable penetrating background in the SWIA data. Such particle population adds a very hot but tenuous component with zero bulk velocity to these observations. Even though this component artificially increases the density and decreases the flow velocity, it is not expected to strongly affect the overall results presented in Figure 1.

The trajectory of MAVEN during the analyzed time interval is displayed (light blue curve) in cylindrical MSO coordinates in Figure 2 (lower panel). Color-coded points display MAVEN's position every 25 minutes. This panel also shows the average location of the BS (solid black line) and the magnetic pile-up boundary (dashed black line), based on the fits by Trotignon et al. [2006]. The initial position of MAVEN is marked by the blue dot closest to the black arrow.

3.2. Global properties derived from LatHyS

Boundaries geometry and location: bow shock and magnetic pile-up boundary

Several factors influence the state of the Martian magnetosphere. In particular, previous studies have investigated the effects that changes in the external/internal electromagnetic field and plasma properties (e.g., the solar wind magnetosonic Mach number, the solar wind dynamic pressure, the IMF cone angle, the crustal magnetic fields, and the extreme ultraviolet flux reaching the Martian atmosphere) have on the location of the Martian bow shock and the magnetic pile-up boundary [e.g., Crider et al., 2003; Edberg et al., 2008, 2009, 2010; Hall et al., 2016]. The three stationary simulations allow us to characterize effects that the solar wind magnetosonic Mach number (M_{MS}) and the solar wind

dynamic pressure (P_{dyn}) have on the bow shock and MPB location, given that these three simulations were performed for the same solar extreme ultra-violet conditions, and with an IMF mainly oriented along the Y_{MSO} axis. To compute the simulated bow shock position in each simulation and to also compare it with previous observational results [Trotignon et al., 2006], the following automatic detection criterion has been applied. For a given Y_{MSO} value, we search along the X_{MSO} axis the position where the magnitude of the magnetic field normalized by the IMF magnitude exceeds a factor 2. The first value starting from $X_{MSO}=2.4 R_M$ towards the planet (that is along the $-X_{MSO}$ direction) is identified as the bow shock location for such Y_{MSO} coordinate. The same criteria has been used to compute the location of the bow shock in the $(X-Z)_{MSO}$ plane, for each given Z_{MSO} value. A pressure balance criterion between solar wind thermal and dynamic pressures leads to a similar result in the subsolar region. It fails on the flanks, however, because the magnetosheath plasma is accelerated flankward and tailward and a simple pressure balance condition is often poorly fulfilled in this region. A similar criterion has been used to compute the MPB location. For each given Y_{MSO} or Z_{MSO} value, we search along the X_{MSO} axis the position where the magnitude of the magnetic field normalized by the IMF magnitude exceeds a factor 6 and the magnitude of the mean plasma velocity normalized by that of the pristine solar wind is reduced by a factor 2. The identified bow shock and MPB locations in the XY and XZ MSO planes (for the three simulations) are shown over-imposed in the left and right upper panels in Figure 2, respectively. The simulated MPB profile cannot be completely recovered because the used criteria is not fulfilled everywhere in the simulation box. However, the derived MPB location is ex-

tended enough to compare it with previous results. According to Trotignon et al. [2006]; Edberg et al. [2008], the average MPB standoff distance varies between $1.25 \pm 0.03 R_M$ and $1.33 \pm 0.15 R_M$. As shown in the Figure 2 (upper right panel), all simulated MPB positions have associated stand-off distances within such distance range. It is also worth noticing that the computed MPB section close to the terminator plane is significantly closer to the planet when comparing Simulations 2 and 3 with Simulation 1 (close to nominal conditions). This suggests a compression on the MPB flanks, as a result of the solar wind dynamic pressure and magnetosonic Mach number increase between these simulations (see corresponding values in Table 1). Interestingly, both MPB flank crossings observed by MAVEN that can be accurately determined during the analyzed time interval support such conclusion. Indeed, the blue and red encircled crosses shown in upper right panel (Figure 2) displayed the cylindrical MSO radial distance and the X_{MSO} coordinate of such MPB crossings, that took place during the first and second orbits. It is worth mentioning that three additional dayside MPB crossings took place during the analyzed time interval. However, the relatively large magnetic field fluctuations in the magnetic field data as well as the variable plasma composition along MAVEN's trajectory inside the Martian magnetosphere prevent us from accurately determining the MPB crossing location in these cases.

Given that the determined simulated bow shock profiles are much more extended, we can compute conic section fits to model the bow shock location assuming cylindrical symmetry along the X_{MSO} axis and using the same methodology reported in Trotignon et al. [2006]. The conic section is defined by:

$$r = L - \varepsilon r \cos(\theta) \quad (1)$$

where r and θ are the polar coordinates expressed from the conic focus, such that $x - x_F = r \cos(\theta)$ and ε , x_F and L are the eccentricity, the focus position along the X axis, and the semi-latus rectum (distance of the shock to the focus in the plane perpendicular to the x-axis), respectively. The derived values for each of these parameters and the R^2 value associated with the linear fit (from Equation 1) for each of the three simulations are presented in Table 1. As can be seen in this Table, the R^2 values are very close to 1, ensuring the derived conic sections fit very well the computed bow shock location derived from LatHyS. The corresponding conic sections are displayed in Figure 2 (lower panel). Based on these fits, we also determined the bow shock stand-off distance and the terminator distance (Table 1). We find the computed terminator distance from each simulation to be consistent with the range of values reported in Edberg et al. [2010]. Indeed, a decreasing trend (although with large scatter) of the extrapolated terminator distance with the M_{MS} was observed in that study, for magnetosonic Mach numbers ranging between 6.1 and 10.5. As shown in Edberg et al. [2009], the solar dynamic pressure has also a strong influence on the location of the bow shock and the magnetic pile-up boundary. An increase in the dynamic pressure was found to push the bow shock downward, and the presence of an asymptote for relatively large dynamic pressure values was suggested (Figure 6, panel a of Edberg et al. [2009]). Consistent with these observations, we find that bow shock fits are very similar (e.g., terminator and stand-off distance) when comparing Simulations 2 and 3 with Simulation 1. That is, a much larger variability in

the bow shock location is found when P_{dyn} varies between 0.58 nPa and 4.54 nPa than when it varies between 4.54 nPa and 13.61 nPa. While the bow shock fit for Simulation 1 is very close to the one reported in Trotignon et al. [2006], the stand off and terminator distances are reduced by $\sim 8\%$ and $\sim 15\%$ percent, respectively, under the conditions for Simulations 2 and 3.

● **H⁺ and O⁺ loss rates**

We also estimate the variability of the H⁺ and O⁺ planetary loss rates between the three LatHyS stationary runs. As can be seen in Table 1, the H⁺ and O⁺ loss rates increase by a factor ~ 10 and ~ 2.4 , respectively, as a result of the changes in the external conditions during the passage of the ICME through the Martian environment (Simulation 1 vs Simulation 3). These increments are mainly the consequence of an increase in the charge exchange ionization rate between solar wind protons and H and O atmospheric neutrals (proportional to $n_{SW} U_{SW}$). Indeed, in both cases this ionization rate increases by a factor ~ 12.2 . In the case of O⁺ escape rates, a significant contribution to such increase is also associated with the motional electric field, that can penetrate to lower altitudes due to the increased solar wind pressure, accelerating and removing ions from the upper layers of the Martian ionosphere. The three LatHyS simulations also show the presence of the O⁺ plume in the positive convective electric field hemisphere, as expected from previous observations [e.g., Dong et al., 2015]. We find that the ratio between the O⁺ escape rate along the convective electric field direction and the total O⁺ escape rate increases from Simulation 1 to Simulation 3. Indeed, as shown in Table 1, this O⁺ escape channel constitutes $\sim 8.5\%$ and $\sim 14.2\%$ of the total O⁺ loss rate for Simulation 1 and

Simulation 3, respectively. O_2^+ and CO_2^+ escape rates are not presented in this paper, since the considered spatial resolution might affect the description of physical processes occurring in the ionosphere. Differences in O^+ computed escape rates between LatHyS and MHD models describing the interaction between ICME events and Mars [e.g., Jakosky et al., 2015b; Ma et al., 2017] might be associated with the considered atmospheric and ionospheric profiles. As mentioned in a previous section, the three LatHyS stationary simulations have used outputs from the LMD-GCM and the EGM codes under mean solar activity conditions and $L_s=90^\circ$. Such differences can also be partly due to the spatial resolution employed to describe the O^+ ionosphere in LatHyS. Previous estimations of planetary ion escape vary significantly due to different factors: the external conditions, instrumental design, considered hypothesis, and/or employed numerical simulation codes, etc, as can be clearly seen for the case of O^+ , in the review by Dubinin et al. [2011]. However, it is worth pointing out that the computed total H^+ ion loss rate for Simulation 1 is approximately twice the one reported in Modolo et al. [2005], under nominal solar wind and solar maximum conditions. The derived total O ion loss rate is close to the one reported in Dong et al. [2015] although, in that work based on MAVEN data, the authors focused only on ions with energies higher than 25 eV. Heavy ion escape rate in the same energy range was analyzed in Brain et al. [2015] and was found to exceed 2×10^{24} ions/s. Comparison of these results with ion escape rates associated with Simulations 2 and 3 support the idea that space weather phenomena are capable of having significant effects on the Martian atmospheric escape. Complementary studies on the interaction between

Mars and other extreme events can better establish the integrated effect of such impacts over the Martian history.

4. Conclusions

In this work we have analyzed the interaction between an ICME and Mars by means of LatHyS stationary runs and MAVEN measurements obtained during mid-September 2017.

Despite that some observations are indicative of the presence of time dependent processes taking place during the analyzed time interval, comparisons between simulated profiles along the spacecraft trajectory and MAVEN MAG, SWIA and STATIC observations show a good agreement. This suggests that several stages during this interaction can be partly described through a combination of steady states. We also find that the simulated bow shock is closer to the planet for higher solar wind dynamic pressure and magnetosonic Mach number conditions, in agreement with previous observational studies. The dayside MPB shows much less variability than the bow shock, although we observe (through MAVEN and LatHyS) a compression on the flanks when the solar wind dynamic pressure and magnetosonic Mach number increase. Finally, we find that the simulated H^+ and O^+ loss rates increase by a factor ~ 10 and ~ 2.4 , respectively, as a result of the ICME passage through the Martian plasma environment.

Acknowledgments. N.R. is supported by a CDD contract from Laboratoires d'excellence Exploration Spatiale des Environnements Planétaires (LABEX-ESEP ANR N° 2011-LABX-030). N.R. is also indebted to the French Space Agency CNES for its support. N.R. would like to thank J. Connerney for useful comments and suggestions. N.R., R.M., F.L. and J-Y.C. are indebted to CNRS for its support on the LIA MAGNETO

and to ANR for the project TEMPETE (ANR-17-CE31-0016). This work is also part of HELIOSARES Project (ANR-09-BLAN-0223) and ANR MARMITE-CNRS (ANR-13-BS05-0012-02). Authors also acknowledge the support of the IPSL data center CICLAD for providing us access to their computing resources. MAVEN data are publicly available through the Planetary Data System (<https://pds-ppi.igpp.ucla.edu/>). Numerical simulations outputs used in this article can be found in <http://impex.latmos.ipsl.fr>.

References

- Acuña, M. H., et al. (1998), Magnetic field and plasma observations at Mars: Initial results of the mars global surveyor mission, *Science*, 279 (5357), 1676-1680.
- Acuña, M. H., et al. (1999), Global distribution of crustal magnetization discovered by the Mars Global Surveyor MAG/ER Experiment, *Science*, 284, 790-793, doi:10.1126/science.284.5415.790.
- Brain, D. A., et al. (2015), The spatial distribution of planetary ion fluxes near Mars observed by MAVEN, *Geophys. Res. Lett.*, 42, 9142-9148, doi:10.1002/2015GL065293.
- Cain, J. C., B. B. Ferguson, and D. Mozzoni, An $n = 90$ internal potential function of the Martian crustal magnetic field, *J. Geophys. Res.*, 108(E2), 5008, doi:10.1029/2000JE001487, 2003.
- Chaufray, J.-Y., F. Gonzalez-Galindo, F. Forget, M. Lopez-Valverde, F. Leblanc, R. Modolo, S. Hess, M. Yagi, P.-L. Blelly, and O. Witasse (2014), Three-dimensional Martian ionosphere model: II. Effect of transport processes due to pressure gradients, *J. Geophys. Res. Planets*, 119, 1614-1636, doi:10.1002/2013JE004551.
- Chaufray, J.-Y., F. Gonzalez-Galindo, F. Forget, M. A. Lopez-Valverde, F. Leblanc, R.

Modolo, and S. Hess (2015), Variability of the hydrogen in the Martian upper atmosphere as simulated by a 3D atmosphere-exosphere coupling, *Icarus*, 245, 282-294, doi:10.1016/j.icarus.2014.08.038.

Chacko, Z., and A. B. Hassam (1997), Steady-state magnetohydrodynamic plasma flow past conducting sphere, *Phys. Plasmas*, 4(8),3031-3039, doi:10.1063/1.872437.

Connerney, J. E. P., J. Espley, P. Lawton, S. Murphy, J. Odom, R. Oliverson, and D. Sheppard (2015a), The MAVEN magnetic field investigation, *Space Sci. Rev.*, 195, 1?35, doi:10.1007/s11214-015-0169-4.

Connerney, J.E.P., Espley, J.R., DiBraccio, G.A., Gruesbeck, J.R., Oliverson, R.J., Mitchell, D.L., Halekas, J., Mazelle, C., Brain, D.A., & Jakosky, B.M. (2015b). First results of the MAVEN magnetic field investigation. *Geophys. Res. Lett.*, 42, 8819-8827, doi:10.1002/2015GL065366.

Crider, D. H., D. Vignes, A. M. Krymskii, T. K. Breus, N. F. Ness, D. L. Mitchell, J. A. Slavin, and M. Acuña, A proxy for determining solar wind dynamic pressure at Mars using Mars Global Surveyor data, *J. Geophys. Res.*, 108(A12), 1461, doi:10.1029/2003JA009875, 2003.

Crider, D. H., J. Espley, D. A. Brain, D. L. Mitchell, J. E. P. Connerney, and M. H. Acuña (2005), Mars Global Surveyor observations of the Halloween 2003 solar superstorm's encounter with Mars, *J. Geophys. Res.*, 110, A09S21, doi:10.1029/2004JA010881.

Curry, S. M., et al. (2015), Response of Mars O⁺ pickup ions to the 8 March 2015 ICME: Inferences from MAVEN data-based models, *Geophys. Res. Lett.*, 42, 9095-9102, doi:10.1002/2015GL065304.

Dong, C., et al. (2015), Multifluid MHD study of the solar wind interaction with Mars' upper atmosphere during the 2015 March 8th ICME event, *Geophys. Res. Lett.*, 42, doi:10.1002/2015GL065944.

E. Dubinin, M. Fraenz, A. Fedorov, R. Lundin, N. Edberg, F. Duru, O. Vaisberg, *Space Sci. Rev.* 162, 173 (2011), doi:10.1007/s11214-011-9831-7

Edberg, N. J. T., M. Lester, S. W. H. Cowley, and A. I. Eriksson (2008), Statistical analysis of the location of the Martian magnetic pileup boundary and bow shock and the influence of crustal magnetic fields, *J. Geophys. Res.*, 113, A08206, doi:10.1029/2008JA013096.

Edberg, N. J. T., D. A. Brain, M. Lester, S. W. H. Cowley, R. Modolo, M. Fränz, and S. Barabash (2009), Plasma boundary variability at Mars as observed by Mars Global Surveyor and Mars Express, *Ann. Geophys.*, 27(9), 3537-3550.

Edberg, N. J. T., M. Lester, S. W. H. Cowley, D. A. Brain, M. Fränz, and S. Barabash (2010), Magnetosonic Mach number effect of the position of the bow shock at Mars in comparison to Venus, *J. Geophys. Res.*, 115, A07203, doi:10.1029/2009JA014998.

Futaana Y. et al., (2008), Mars Express and Venus Express multi-point observations of geo-effective solar flare events in December 2006, *Planetary and Space Science*, Volume 56, Issue 6, 873-880, <http://dx.doi.org/10.1016/j.pss.2007.10.014>.

González-Galindo, F., et al. (2009), A ground-to-exosphere Martian circulation model: 1. Seasonal, diurnal, and solar cycle variation of thermospheric temperatures, *J. Geophys. Res.*, 114, E04001, doi:10.1029/2008JE003246.

Gopalswamy, N. (2006), Properties of interplanetary coronal mass ejections, *Space Sci.*

Rev., 124, 145-168, doi:10.1007/s11214-006-9102-1.

Gosling, J., D. McComas, J. Phillips, and S. Bame (1991), Geomagnetic activity associated with Earth passage of interplanetary shock disturbances and coronal mass ejections, *J. Geophys. Res.*, 96(A5), 7831-7839, doi:10.1029/91JA00316.

Halekas, J. S., E. R. Taylor, G. Dalton, G. Johnson, D. W. Curtis, J. P. McFadden, D. L. Mitchell, R. P. Lin, and B. M. Jakosky (2015), The solar wind ion analyzer for MAVEN, *Space. Sci. Rev.*, doi:10.1007/s11214-013-0029-z.

Halekas, J. S., Brain, D. A., Luhmann, J. G., DiBraccio, G. A., Ruhunusiri, S., Harada, Y., ... Jakosky, B. M. (2017). Flows, fields, and forces in the Mars-solar wind interaction. *Journal of Geophysical Research: Space Physics*, 122, 11, 320-11, 341. <https://doi.org/10.1002/2017JA024772>

Hall, B. E. S., et al. (2016), Annual variations in the Martian bow shock location as observed by the Mars Express mission, *J. Geophys. Res. Space Physics*, 121, 11, 474-11, 494, doi:10.1002/2016JA023316.

Jakosky, B. M., et al. (2015a), The Mars Atmosphere and Volatile Evolution (MAVEN) mission, *Space Sci. Rev.*, 195(1-4), 3-48, doi:10.1007/s11214-015-0139-x.

Jakosky, B. M., et al. (2015b), MAVEN observations of the response of Mars to an interplanetary coronal mass ejection, *Science*, American Association for the Advancement of Science, 2015, 350 (6261), DOI: 10.1126/science.aad0210.

Jian, L. K., C. T. Russell, J. G. Luhmann, R. M. Skoug, and J. T. Steinberg (2008), Stream interactions and interplanetary coronal mass ejections at 5.3 AU near the solar ecliptic plane, *Sol. Phys.*, 250, 375-402, doi:10.1007/s11207-008-9204-x.

Leclercq, L., R. Modolo, F. Leblanc, S. Hess, and M. Mancini (2016), 3D magnetospheric parallel hybrid multi-grid method applied to planet-plasma interactions, *J. Comput. Phys.*, 309, 295-313, doi:10.1016/j.jcp.2016.01.005.

Leblanc, F., Leclercq, L., Oza, A., Schmidt, C., Modolo, R., Chaufray, J. Y., & Johnson, R. E. (2017a). 3D multispecies collisional model of Ganymede's atmosphere. *Icarus*, 293, 185-198. <https://doi.org/10.1016/j.icarus.2017.04.025>

Leblanc, F., Chaufray, J. Y., Modolo, R., Leclercq, L., Curry, S., Luhmann, J., ... Jakosky, B. (2017b). On the origins of Mars' exospheric nonthermal oxygen component as observed by MAVEN and modeled by HELIOSARES. *Journal of Geophysical Research: Planets*, 122, 2401-2428. <https://doi.org/10.1002/2017JE005336>

Lee, C. O. et al (2018), Observations and Impacts of the 10 September 2017 Solar Events at Mars: An Overview, This issue, GRL Submission ID 2018GL077917.

Ma, Y., A. F. Nagy, I. V. Sokolov, and K. C. Hansen (2004), Three-dimensional, multi-species, high spatial resolution MHD studies of the solar wind interaction with Mars, *J. Geophys. Res.*, 109, A07211, doi:10.1029/2003JA010367.

Ma, Y. J., et al. (2017), Variations of the Martian plasma environment during the ICME passage on 8 March 2015: A time-dependent MHD study, *J. Geophys. Res. Space Physics*, 122, 1714-1730, doi:10.1002/2016JA023402.

Ma, Y. et al (2018), The Impact and Solar wind Proxy of the 2017 September ICME Event at Mars, This issue, GRL Submission ID 2018GL077707.

McFadden, J., et al. (2015), The MAVEN Suprathermal and thermal Ion Composition (STATIC) instrument, *Space Sci. Rev.*, 195, 199-256, doi:10.1007/s11214-015-0175-6.

Modolo, R., G. M. Chanteur, E. Dubinin, and A. P. Matthews (2005), Influence of the solar EUV flux on the Martian plasma environment, *Ann. Geophys.*, 23, 433-444, doi:10.5194/angeo-23-433-2005.

Modolo, R., G. M. Chanteur, and E. Dubinin (2012), Dynamic Martian magnetosphere: Transient twist induced by a rotation of the IMF, *Geophys. Res. Lett.*, 39,L01106, doi:10.1029/2011GL049895.

Modolo, R., et al. (2016), Mars-solar wind interaction: LatHyS, an improved parallel 3-D multispecies hybrid model, *J. Geophys. Res. Space Physics*, 121, 6378-6399, doi:10.1002/2015JA022324.

Morgan, D. D., et al. (2014), Effects of a strong ICME on the Martian ionosphere as detected by Mars Express and Mars Odyssey, *J. Geophys. Res. Space Physics*, 119, 5891-5908, doi:10.1002/2013JA019522.

Y. Naor and U. Keshet (2015), Magnetohydrodynamics using path or stream functions, *ApJ*, 810, 152.

Richer, E., R. Modolo, G. M. Chanteur, S. Hess, and F. Leblanc (2012), A global hybrid model for Mercury's interaction with the solar wind: Case study of the dipole representation, *J. Geophys. Res.*, 117, A10228, doi:10.1029/2012JA017898.

Romanelli, N., D. Gómez, C. Bertucci, and M. Delva (2014), Steady-state magnetohydrodynamic flow around an unmagnetized conducting sphere, *Astrophys. J.*, 789(1), 43.

Romanelli, N., C. Bertucci, D. Gómez, and C. Mazelle (2015), Dependence of the location of the Martian magnetic lobes on the interplanetary magnetic field direction: Obser-

vations from Mars Global Surveyor, *J. Geophys. Res. Space Physics*, 120, 7737-7747, doi:10.1002/2015JA021359.

Russell, C.T., Elphic, R.C., Slavin, J.A., (1980). Limits on the possible intrinsic magnetic field of Venus. *J. Geophys. Res.* 85 (December), 8319-8332.

Sánchez-Cano, B., et al. (2017), Mars plasma system response to solar wind disturbances during solar minimum, *J. Geophys. Res. Space Physics*, 122, 6611-6634, doi:10.1002/2016JA023587.

Thiemann, E. M. B. et al (2018), The Mars Upper Ionosphere Response to the X8.2 Solar Flare of 10 September 2017, This issue, GRL Submission ID 2018GL077730.

Trotignon, J. G., C. Mazelle, C. Bertucci, and M. H. Acuña (2006), Martian shock and magnetic pile-up boundary positions and shapes determined from the Phobos 2 and Mars Global Surveyor data sets, *Planet. Space Sci.*, 54, 357-369, doi:10.1016/j.pss.2006.01.003.

Tsurutani, B., and W. Gonzalez (1997), The interplanetary causes of magnetic storms: A review, in *Magnetic Storms*, vol. 98, edited by B. Tsurutani et al., pp. 77-89, *Geophys. Mon. Series*, Washington, D. C.

	Simulation 1	Simulation 2	Simulation 3
Time interval	2017-09-12 22:00 UT - 2017-09-13 02:52 UT	2017-09-13 02:52 UT - 2017-09-13 05:10 UT	2017-09-13 05:10 UT - 2017-09-13 08:20 UT
n_{SW} (cm^{-3})	1.9	4	12
\mathbf{U}_{SW} (km/s)	(-426,0,0)	(-824,0,0)	(-824,0,0)
\mathbf{B}_{IMF} (nT)	(0,-3,0)	(0,-10,0)	(0,10,5)
M_{MS}	5.15	6.40	8.40
P_{dyn} (nPa)	0.58	4.54	13.61
Bow shock parameters: ε , $L(\mathbf{R}_M)$, $x_F(\mathbf{R}_M)$	0.983, 2.195, 0.53	0.915, 1.801, 0.58	0.907, 1.810, 0.55
R^2	0.995	0.998	0.997
Bow shock stand-off distance (\mathbf{R}_M)	1.64	1.52	1.50
Bow shock terminator distance (\mathbf{R}_M)	2.66	2.26	2.24
O^+ escape (10^{24} ions/s)	1.3	1.9	3.1
O^+ escape along the convective electric field (10^{23} ions/s)	1.1	1.9	4.4
H^+ escape (10^{25} ions/s)	2.1	8.2	21.9

Table 1. Solar wind properties, IMF, magnetosonic Mach number and SW dynamic pressure considered for each of three simulations during the corresponding time interval. Bow shock properties derived from fits to LatHyS results and estimated planetary O^+ and H^+ escape rates are also presented.

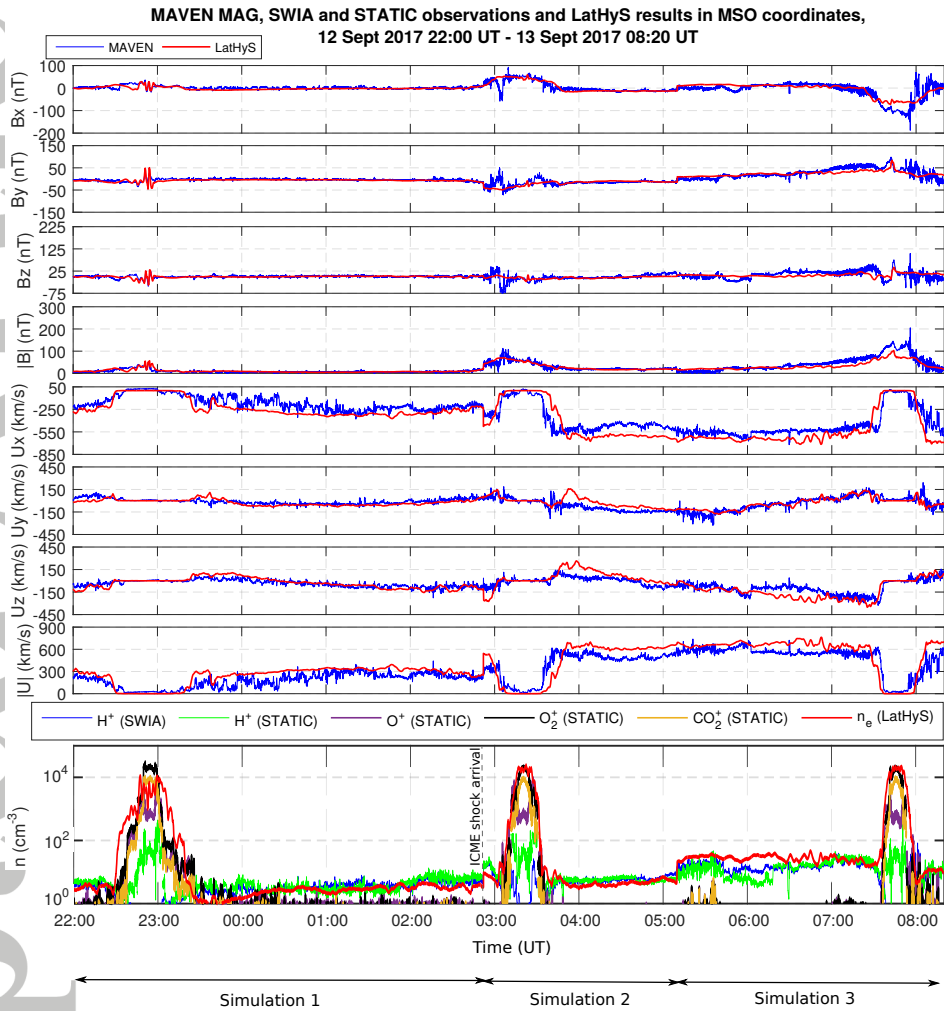


Figure 1. LathYS results and MAVEN MAG, SWIA and STATIC observations between 12 September 2017, 22:00 UT and 13 September 2017, 08:20 UT. From top to bottom: the magnetic field MSO components and magnitude, the SWIA MSO bulk plasma velocity components and magnitude, and the SWIA and STATIC ion densities.

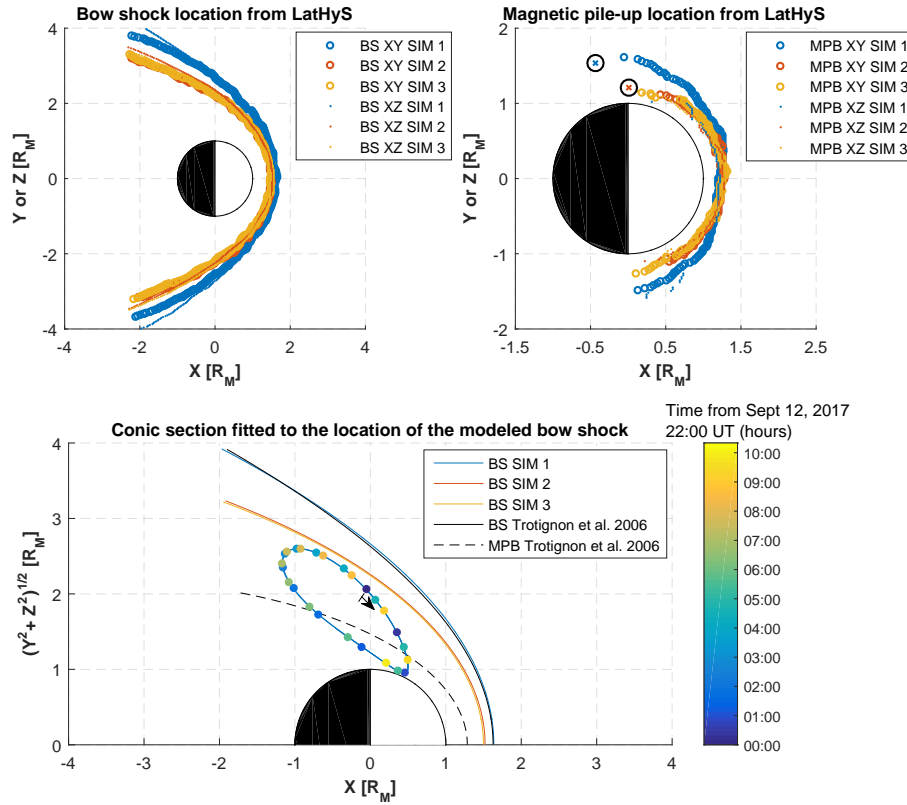


Figure 2. Bow shock and magnetic pile-up location from LathyS. Upper left (right) panel: bow shock (magnetic pile-up boundary) location in the X-Y and X-Z MSO planes for the three stationary simulations. The upper right panel also shows two MPB flank crossings from MAVEN observations (encircled crosses), see text. Lower panel: Conic section fitted to the location of the modeled bow shock in each of the three simulations, in cylindrical MSO coordinates. Bow shock and magnetic pile-up boundary derived in Trotignon et al. [2006] are also shown, for easy comparison. MAVEN trajectory between 12 September 2017, 22:00 UT and 13 September 2017, 08:20 UT is also shown in light blue. The color-coded points display the position of MAVEN at a particular time, every 25 minutes approximately.